Micron-Scale Photodetectors Based on One-Dimensional Single-Crystalline Sb2-xSnxSe3 Microrods Simultaneously Improving Responsivity and Extending Spectral Response Region

X. Luo, S. Chen, L. Liu, J. Lv, A. Qadir, K. Shehzad, X. Qiao, Y. Xu, L. Kienle, A. Lotnyk, et al.

Micron Scale Photo-detectors Based-on 1D Single Crystalline $Sb_{2-x}Sn_xSe_3$ Micro-rods: Simultaneously Improving Responsivity and Extending Spectral Response Region

Xue Luo,[a] Shuo Chen,[a] Lixiang Liu,[b] Jianhang Lv,[b] Akeel Qadir,[b] Khurram Shehzad,[b] Xvsheng Qiao,[a,*] Yang Xu,[a,b,*] Lorenz Kienle,[c] Andriy Lotnyk,[d] Xianghua Zhang,[e] Guodong Qian,[a] Xianping Fan[a,*]

[a] *State Key Laboratory of Silicon Materials & School of Materials Science and Engineering, Zhejiang University, Hangzhou, 310027, P. R. China.*

[b] *School of Information Science and Electronic Engineering, Zhejiang University, Hangzhou, 310027, P. R. China*

[c] *Institute for Material Science, Synthesis and Real Structure, Christian Albrechts University Kiel, Kaiserstr. 2, 24143 Kiel, Germany*

[d] *Leibniz Institute of Surface Engineering (IOM), Permoserstr. 15, 04318 Leipzig, Germany*

[e] *Laboratory of Glasses and Ceramics, Institute of Chemistry, CNRS-Université de Rennes I, Campus de Beaulieu, 35042 Rennes cedex, France*

ABSTRACT

Among various 1D materials, antimony selenide (Sb_2Se_3) has the large visible to near-infrared (Vis-NIR) absorption cross section and excellent stability, thus it shows a huge potential to be applied as photodetectors. However, low electrical conductivity ($10^{-6}\ \Omega^{-1}\cdot m^{-1}$ in bulk state) largely limits the extensive applications of Sb_2Se_3. By a hot-injection based Sn/Sb substitution strategy,

we prepare 1D $Sb_{2-x}Sn_xSe_3$ micro-rods in order to further improve photodetecting performances of Sb_2Se_3 micro-rods. Phase and microstructural analysis revealed the formation of orthorhombic 1D $Sb_{2-x}Sn_xSe_3$ micro-rods with the length of 20 ~ 30 μm. From Hall Effect measurements and absorption spectra, the $Sb_{2-x}Sn_xSe_3$ micro-rods were evidenced as a p-type semiconductor with a higher electrical conductivity ($6.95 \times 10^{-4}\ \Omega^{-1}\cdot m^{-1}$) and a smaller band gap (0.97 eV) compared with Sb_2Se_3 micro-rods. Accordingly, the photodetector based on a single $Sb_{2-x}Sn_xSe_3$ micro-rod exhibited a remarkable response to 980 nm light at 10 V with a high responsivity (1.84×10^4 $A\cdot W^{-1}$), a fast response/recovery time (0.134 s/0.153 s) and a long-term durability. Due to the small bandgap, the photodetector also exhibited a broadband photoresponse at Vis-NIR spectral range. Given their high-responsivity and broadband response, the photodectector based on a single $Sb_{2-x}Sn_xSe_3$ micro-rod is a promising candidate for applications in next-generation micro-devices.

INTRODUCTION

One-dimensional (1D) semiconductor micro-/nano-materials are promising candidates for achieving high-performance micron-scale photodetector devices because of their large surface-to-volume ratio, small Debye length comparable to their radius, short diffusion-to-surface time with respect to electron-to-hole recombination times and almost perfect crystalline quality. [1-3] Among various 1D materials, antimony selenide (Sb_2Se_3) exhibits a huge potential to obtain high responsivity, fast response speed and excellent stability when applied as photodetectors.[4, 5] These superior characteristics are attributed to the large visible to near-infrared (Vis-NIR) absorption cross section,[4] the narrow band gap [6] and the specific features [7, 8] of the 1D orthorhombic crystal structure of Sb_2Se_3. The optical band gap of single-crystalline Sb_2Se_3 is 1.11 eV and the absorption

coefficient reaches as high as 10^5 cm^{-1} in the Vis-NIR spectral region. The Sb_2Se_3 crystals can be easily grown as 1D-oriented micro-rods or nano-rods, where the structural units of covalently bonded $(Sb_4Se_6)_n$ are stacked by Van der Waals' force. However, low electrical conductivity (10^{-6} $\Omega^{-1}\cdot m^{-1}$ in bulk state) largely limits the extensive applications of Sb_2Se_3 for high-performance photodetection.[5] To solve the problem, various strategies have been employed to improve the electrical conductivity of Sb_2Se_3-based materials. These strategies include controlling rod diameter, [5] decorating with Ag_2S, [5] incorporating Bi into Sb_2Se_3 [9] and fabricating Sb_2Se_3/Cu_2GeSe_3 [4] or $Sb_2Se_3/AgSbSe_2$ [10] heterojunctions.

Energy band engineering is an effective strategy to tune the electrical and photoelectrical performances of semiconductors, which has been widely applied in the semiconductor industry[11, 12]. Hereby, a strategy by Sn/Sb substitution is applied to improve the electrical conductivity and to extend the photoresponse spectral region. Such strategy has been well evidenced in some previously reported literature. M. S. Iovu et al.[13] reported that the electrical conductivity and photoconductivity of the amorphous As_2Se_3 films could have an outstanding increase after introducing a small amount of Sn. Ankit et al.[14] also claimed that increasing the Sn content in $Ge_{1-x}Sn_x/Ge$ induced a significant bandgap shrinkage, thus extending the photodetecting range. Therefore, to form $Sb_{2-x}Sn_xSe_3$ through Sn/Sb substitution might be a suitable energy band engineering strategy to improve the photodetecting performance.

In our previous study, we have reported the enhanced electrical conductivity and photoconductive properties of Sn-doped Sb_2Se_3 bulk crystals. [12] In the present study, we fabricate 1D single-crystalline $Sb_{2-x}Sn_xSe_3$ micro-rods by Sn/Sb substitution to apply Sb_2Se_3 as a micron-scale photodetector and improve its performance. After introducing Sn, the carrier concentration of $Sb_{2-x}Sn_xSe_3$ is largely improved up to 6.139×10^{13} cm^{-3}. The prepared $Sb_{2-x}Sn_xSe_3$ micro-rods

exhibit a much higher electrical conductivity than pure Sb_2Se_3 micro-rods. As the result, the photo-detector based on a single $Sb_{2-x}Sn_xSe_3$ micro-rod shows high responsivities, relatively short response times and extended response to the NIR region.

EXPERIMENTAL DETAILS

Materials

The materials used were: Selenium powder (Alfa Aesar, 99.5%), Antimony (III) acetate (Sigma-Aldrich, 99.99%), Tin (III) acetate (Alfa Aesar, 95%), Oleic acid (Sigma-Aldrich, 90%), ethylene diamine (Sigma-Aldrich, ReagentPlus ≥ 90%), and oleylamine (Aladdin, C18：80%-90%).

Characterization

X-ray diffraction (XRD) analysis was carried out on a PANalytical B.V. Empyrean 200895 X-ray diffractometer at a scanning rate of 2° min^{-1}, using Cu Kα radiation (λ = 1.54 Å). The morphology of the synthesized micro-rods was characterized under a Hitachi S-4800 field emission scanning electron microscope. TEM, HRTEM images and the corresponding EDS mapping characterization were performed with an FEI Tecnai G2F20 field emission transmission electron microscope operating at an acceleration voltage of 200 kV. The performance of the device was measured by a Keithley 4200 SCS at room temperature in air, and the light sources are single lasers (532, 980, and 1319 nm). X-ray photoelectron spectroscopy (XPS, ESCALAB) was used to analyze the element composition of the micro-rods. The absorption spectra were acquired using a SHIMADZU UV-3150 spectrophotometer. Finally, the electrical properties of the micro-rods were investigated by the Hall Effect measurement with (BID-RAD HL5500PC) at room temperature. Before the Hall Effect measurement, the as-prepared micro-rods powder was pressed into a dense wafer with

diameter of about 1 cm and thickness of about 0.4 mm, then silver paint as electrodes was applied at four symmetric corners on one face of the wafer for ohmic contacts.

Synthesis of Sb_2Se_3 micro-rods.

Sb_2Se_3 micro-rods were synthesized by a simple solvothermal method with slight modifications. In specific, 1.0 mmol of $Sb(Ac)_3$ and 0.3 mmol of selenium powder were dissolved in 18 mL of ethylenediamine and 6 mL oleic acid and stirred for 30 min. Then the mixture was transferred into an autoclave (volume 30 mL) and stored in the oven at 210 °C for 12 h. After cooling to room temperature, the products were collected by centrifugation at 4000 rpm for 3 min, washed three times with ethanol, and finally dried at 60 °C in a vacuum oven.

Synthesis of $Sb_{2-x}Sn_xSe_3$ micro-rods through Sn/Sb substitution of Sb_2Se_3 micro-rods.

$Sn(Ac)_2$ (0.1 mmol) was added to 8 mL of oleylamine (OM) in a 50 mL three-neck flask. The slurry was degassed upon heating at 120 °C under vacuum with vigorous magnetic stirring for 30 min. The mixture was purged with argon and heated to 150 °C to produce a clear yellow solution. Then, 1.0 mmol of the Sb_2Se_3 micro-rods dispersion with 4 mL of OM as solvent was rapidly injected into the aforementioned solution. The mixture was cooled to room temperature after reacting for 10 min. The obtained $Sb_{2-x}Sn_xSe_3$ micro-rods were collected by centrifugation, washed three times with alcohol, and finally dried at 60 °C in a vacuum oven.

Fabrication of a single-micro-rod photodetector

A single-micro-rod photodetector device was fabricated by a micro-mechanical method. Au electrodes were fabricated on SiO_2/Si substrates using phaloetching[15]. Micro-rods were dispersed in alcohol and the solution was drop-casted on the silicon wafer. Subsequently, the

polydimethylsiloxane (PDMS) membrane was adhered to a glass transfer slide, which was clamped onto the arm of a micromanipulator mounted on an optical microscope. The single micro-rod that is suspended on the silicon wafer was optically located using a microscope, the glass was controlled to touch the selected micro-rod, and then the silicon wafer was heated to 100°C to partially melt the PDMS membrane and allow the micro-rod to adhere onto the PDMS membrane. Finally, the micro-rod was transferred to the Au electrode, and the target substrate was heated to 180°C to melt the PDMS membrane and facilitate the alignment of the micro-rod to the Au electrode.

RESULTS AND DISCUSSION

The $Sb_{2-x}Sn_xSe_3$ micro-rods are well affirmed through the phase and microstructure identifications. It corroborates the feasibility of the Sn/Sb substitution strategy. The XRD results shown in Figure 1(a) confirm (with JCPDS Card, No. 65-1317) the orthorhombic phase of the Sb_2Se_3 micro-rods. By contrast, the diffraction of the $Sb_{2-x}Sn_xSe_3$ micro-rods (Figure 1(b)) are slightly shifted to a larger 2θ angle compared with those of pure Sb_2Se_3. This finding implies that the lattice of the $Sb_{2-x}Sn_xSe_3$ micro-rods experiences a small distortion owing to the atomic radius difference between Sb (0.160 nm) and Sn (0.158 nm).[16] Figure 1(b) shows the relatively enlarged detail of the (302), (112), (212) and (013) reflections. SEM images of the Sb_2Se_3 and $Sb_{2-x}Sn_xSe_3$ micro-rods (Figure 1 (c-d)) appear no obvious change in morphology. Both of them have a smooth surface with a uniform diameter of 1-2 μm and a typical length of 20-30 μm. HRTEM images (Figure 1 (e-f)) and the corresponding selected-area electron diffraction patterns (inset images) indicate that Sb_2Se_3 and $Sb_{2-x}Sn_xSe_3$ have a highly ordered single crystalline nature with clearly displayed [001] growth directions and d (001) – spacings of 0.396 and 0.392 nm, respectively.

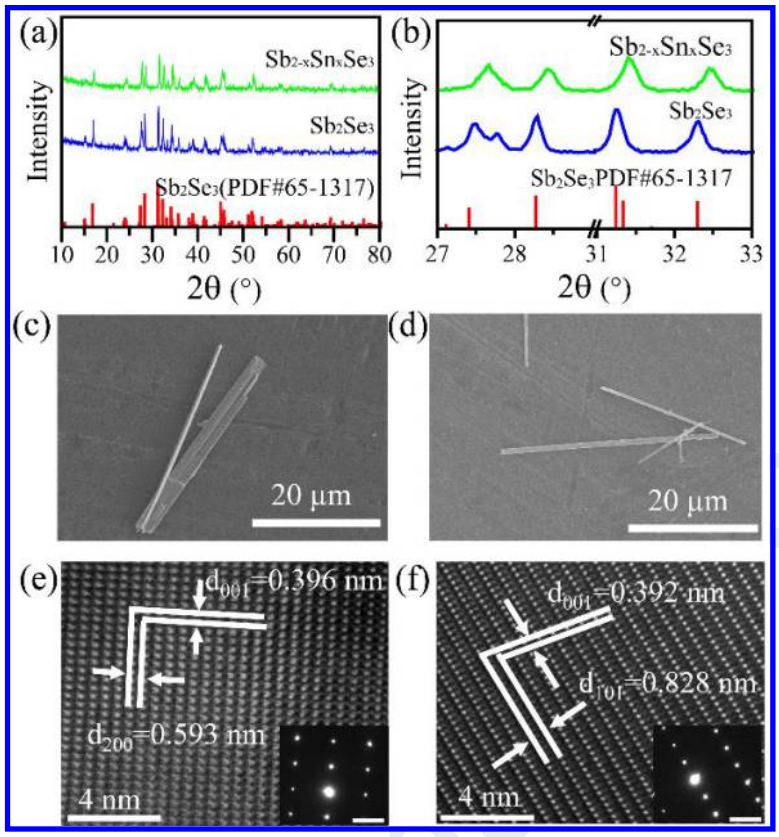

Figure 1. (a) XRD patterns of Sb_2Se_3 micro-rods and $Sb_{2-x}Sn_xSe_3$ micro-rods, (b) partial enlarged detail of figure (a); SEM image of (c) Sb_2Se_3 micro-rods and (d) $Sb_{2-x}Sn_xSe_3$ micro-rods; HRTEM image of (e) Sb_2Se_3 micro-rods and (f) $Sb_{2-x}Sn_xSe_3$ micro-rods. The insets are the electron diffraction patterns by Fast Fourier Transforming (FFT) of the selected area corresponding to (e) and (f), where the scale bars stand for 2 1/nm.

Elemental analysis provides further evidences of the formation of $Sb_{2-x}Sn_xSe_3$ micro-rods. Under High Angle Annular Dark field (HAADF) scanning TEM (STEM) (Figure 2 (a)), the energy- dispersive X-ray (EDX) elemental maps (Figure 2 (b-d)) reveal that Sb, Sn and Se are homogenously distributed in the whole $Sb_{2-x}Sn_xSe_3$ micro-rod. Sb and Se have high filling density and appear within the same energy range. Sn has been introduced in low concentration and sparsely disperses in the micro-rod. The distribution region also exceptionally extends as a cladding of the micro-rod, corresponding to the coronal structure at the surface of the micro-rod. That may be the residual substance from the Sn/Sb substitution process. On the EDX spectra (Figure 2(e)), the

$Sb_{2-x}Sn_xSe_3$ micro-rod exhibits strong Sb and Se peaks. In addition the Sn peaks can be observed by magnifying the region of 24~27 KeV (Figure 2 (f)). It also implies the effective Sn/Sb substitution of Sn into the micro-rod, and the value of x can be determined as 0.163. Similarly, the EDX spectrum (Figure S1†) only reveals strong Sb and Se peaks (no Sn peak). Expectedly, the atomic ratio of Sb and Se is close to the intrinsic 2:3 stoichiometry. X-ray photoelectron spectroscopy (XPS) further confirm the existence of Sn^{4+} in the $Sb_{2-x}Sn_xSe_3$ micro-rods. As shown in Figure 3, two XPS peaks of the $Sb_{2-x}Sn_xSe_3$ micro-rods are observed at 485.9 and 494.5 eV. These peaks could be assigned to Sn^{4+}, referenced by the previously reported data. [17]

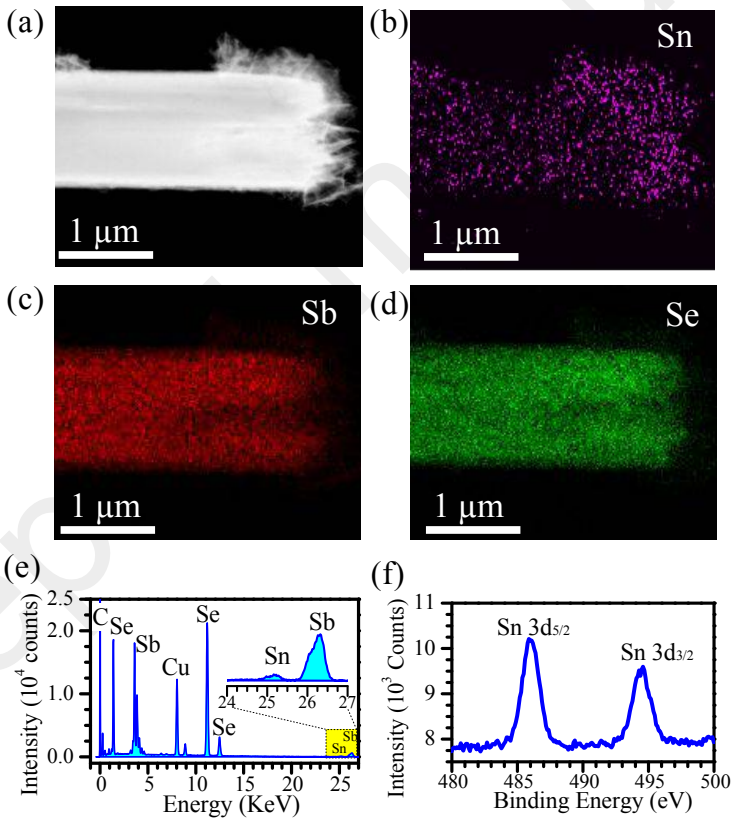

Figure 2. (a) High Angle Annular Dark field (HAADF) image of the single $Sb_{2-x}Sn_xSe_3$ micro-rod; EDX maps of Sn (b), Sb (c), and Se (d) elements; EDX spectrum (e) and XPS spectrum (f) of the single $Sb_{2-x}Sn_xSe_3$ micro-rod.

Table 1. Electrical properties of the synthesized Sb_2Se_3 micro-rods and $Sb_{2-x}Sn_xSe_3$ micro-rods.

Sample	Resistivity (Ω·m)	Electrical conductivity ($\Omega^{-1}\cdot m^{-1}$)	Hall mobility ($cm^2\cdot V^{-1}\cdot s^{-1}$)	Carrier concentration (cm^{-3})	Conduction type
Sb_2Se_3 micro-rods	6.048×10^3	1.65×10^{-4}	3.22	3.201×10^{12}	p-type
$Sb_{2-x}Sn_xSe_3$ micro-rods	1.439×10^3	6.95×10^{-4}	0.706	6.139×10^{13}	p-type

The introduction of Sn into Sb_2Se_3 improves its electrical conductivity which is expected to increase the photodetecting performance of $Sb_{2-x}Sn_xSe_3$ micro-rods. Table 1 lists the typical electrical properties of the investigated micro-rods. The $Sb_{2-x}Sn_xSe_3$ micro-rods have an electrical conductivity up to $6.95 \times 10^{-4}\ \Omega^{-1}\cdot m^{-1}$, which is four times higher than the value of 1.65×10^{-4} measured for the Sb_2Se_3 micro-rods. By a Sn/Sb substitution strategy, Sn substitutes Sb to produce $Sn_{Sb}^{\times}$ acceptors. They release hole electronic defects and endow $Sb_{2-x}Sn_xSe_3$ micro-rods as a p-type semiconductor with generating extra carriers (holes).The chemical reaction can be written as：

$$Sn^{2+} + C_{18}H_{35}NH_2 + 2H_2O \rightarrow Sn^{4+} + C_{18}H_{35}NH_4 + 2OH^- \quad (1)$$

$$Sb_2Se_3 + Sn^{4+} \rightarrow SbSnSe_3 + Sb^{3+} + h^{\cdot} \quad (2)$$

As a result, $Sb_{2-x}Sn_xSe_3$ shows a carrier concentration (6.139×10^{13} cm^{-3}) about 20 times as high as that of the pure Sb_2Se_3 (3.201×10^{12} cm^{-3}). It eventually helps $Sb_{2-x}Sn_xSe_3$ to obtain a high electrical conductivity. Hence, the $Sb_{2-x}Sn_xSe_3$ micro-rods are expected to achieve high optoelectronic properties, such as large photo-current and high responsivity.

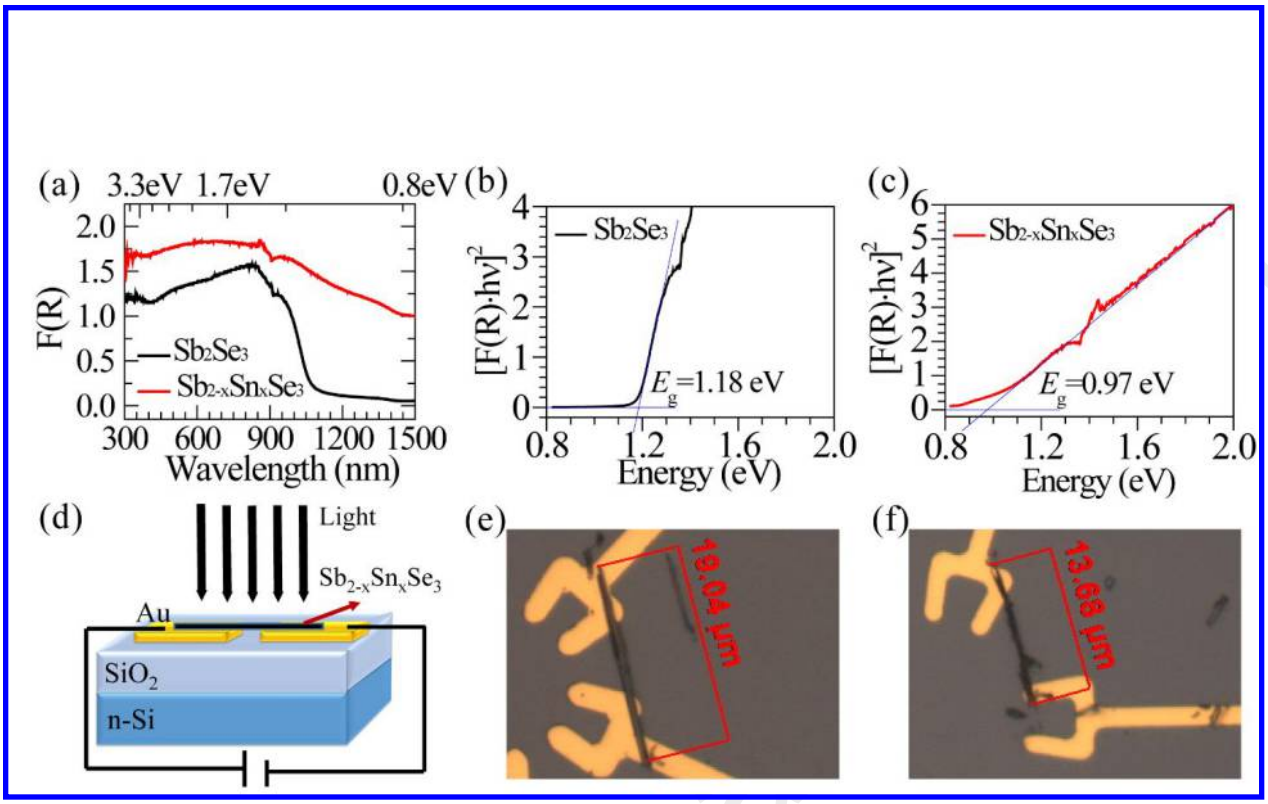

Figure 3. Optical absorption spectra (a) (calculated from the diffuse reflectance data) for Sb_2Se_3 and $Sb_{2-x}Sn_xSe_3$ micro-rods; a plot of [F(R) $h\nu$]^2 vs. energy for the Sb_2Se_3 micro-rods (b) and $Sb_{2-x}Sn_xSe_3$ micro-rods (c), from which band gap energy could be evaluated; schematic illustration of a single micro-rod photodetector (d); optical images of fabricated devices based on a single Sb_2Se_3 micro-rod (e) and based on a single $Sb_{2-x}Sn_xSe_3$ micro-rod (f).

Another important influence of the Sn/Sb substitution is to induce a band gap shrinkage of the $Sb_{2-x}Sn_xSe_3$ micro-rods (E_g = 0.97 eV), which declines to be smaller than that of the Sb_2Se_3 micro-rods (E_g = 1.18 eV). Those have been depicted as Figure 3, where both the absorption of Sb_2Se_3 and $Sb_{2-x}Sn_xSe_3$ micro-rods show a wide absorption region from visible to NIR regions. The ripples around 800~900 nm are caused by the detector change of the spectrophotometer. As the Sb_2Se_3 owns a direct gap, the bandgap (E_g) can be determined as the horizontal interception value of the plot of [F(R)$h\nu$]^2 versus energy yield. In a previous report, [18] $SnSe_2$ has an indirect bandgap of 0.79 eV. We believe it is reasonable for $Sb_{2-x}Sn_xSe_3$ to show an intermediate band gap of 0.97

eV between 1.15 eV (Sb_2Se_3) and 0.79 eV ($SnSe_2$). Thus, $Sb_{2-x}Sn_xSe_3$ micro-rods can find important optoelectronic applications in the infrared spectral region.

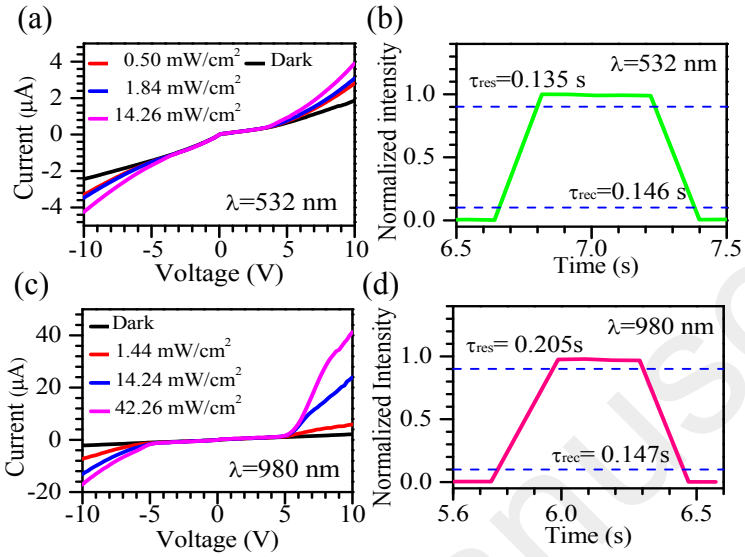

Figure 4. Photoconductive performance of the photodetector based on the single Sb_2Se_3 micro-rod. (a) Dark current and photo-currents under 532 nm irradiation with different incident power densities; (b) An "on/off" cycle under 532 nm irradiation with 71.35 mW·cm^{-2} power density to show response and recovery time at a bias of 10V; (c) Dark current and photo-currents under 980 nm irradiation with different incident power densities; (d) An "on/off" cycle under 980 nm irradiation with 74.23 mW·cm^{-2} power density to show response and recovery times at a bias of 10V.

The working mechanism of photoconductive photodetectors is mainly based on the intrinsic or impurity photoconductive effects in semiconductor materials. When semiconductor materials is irradiated with a light beam, photons with energy larger than the band gap will be absorbed to excite electrons from valence band or impurity energy levels to the conduction band and produce free electron-hole pairs. This will increase the carrier concentration, resulting in an increase in the conductivity. If the voltage bias is applied to such photoconductive materials, the metrics between photocurrent and irradiation intensity can be accordingly established to evaluate the photon energy.

To demonstrate the improved performance of crystalline $Sb_{2-x}Sn_xSe_3$ micro-rods over Sb_2Se_3 micro-rods, we connected the micro-rods with Au Schottky contact electrodes to fabricate photodetector micro-devices on SiO_2/Si substrates. Figure 3(d-f) displays the schematic configuration and top-view microscopy images of such micro-rod-based photodetector. The length and diameter of the single Sb_2Se_3 micro-rod (Figure 3(e)) are 18.14 and 1.46 μm, respectively. Thus the effective illumination area is 26.53 μm^2. Similarly, the area of the single $Sb_{2-x}Sn_xSe_3$ micro-rod (Figure 3(f)) is evaluated as 18.16 μm^2 (length of 13.68 μm and diameter of 1.33 μm). Figure 4 shows the I-V curves of the single Sb_2Se_3 micro-rod photodetector under dark and light irradiation conditions. Figure 4(a, c) shows two characteristics of back-to-back Schottky contacts at the two ends of the Sb_2Se_3 micro-rod. The dark current is as small as −2.5 μA at −10 V which agrees well with the large electric resistivity of the Sb_2Se_3 micro-rods (6.048×10^3 Ω·m). Upon 532 nm laser illumination, the photo-current reaches up to > 4μA at 10 V with the increased light power density (14.26 mW/cm^2). Similarly, upon the 980 nm laser illumination, the photo-current could reach −12 μA at −10 V with the light power density of 14.24 mW/cm^2. The photo-current is three times higher than that of 532 nm illumination. The relatively large photo-response of the Sb_2Se_3 micro-rod could be attributed to the accouplement of 980 nm with its band-gap (1.18 eV). Furthermore, high response and recovery speed are necessary for optical switching device application. These two factors are respectively defined as the response time (time required for the photocurrent to rise from 10% to 90%) and the recovery time (time required for photocurrent to drop from the 90% to 10%). As shown in Figure 4(b, d), response time (τ_{res}) of 0.135 s and recovery time (τ_{rec}) of 0.146 s were obtained at 532 nm, and τ_{res} = 0.205 s and τ_{rec} = 0.147 s were obtained at 980 nm, those error bars are listed in Table S2 and Table S3. Those values are shorter compared with some previously reported results.[19, 20] In addition, the Sb_2Se_3 micro-rod photodetector

demonstrates good repeatability and stability on time-resolved photo-response behaviours (see Figure S2 (a-b)). Therefore, the as-synthesized Sb_2Se_3 micro-rod has better photodetecting performance than bulk Sb_2Se_3 alloys. This finding can be attributed to the following reasons. First, improved field-emission and electron transport properties were achieved due to the good crystal quality and largely reduced number of grain boundaries and/or other interfaces in single-crystalline Sb_2Se_3 micro-rods. Second, with the large surface-to-volume ratio of micro-rods, electron transport can be significantly influenced by surface adsorbates[21, 22], which significantly reduces the scattering, trapping, and the transit time between electrodes during transport.

The $Sb_{2-x}Sn_xSe_3$ micro-rod exhibits even better photoelectronic performances compared with the Sb_2Se_3 micro-rod. Photoelectronic experiments were performed under 532, 980 and 1319 nm laser illumination, and excellent photo-response performance can be observed in the visible to NIR region, as shown in Figure 5. Compared with the photodetector based on a single Sb_2Se_3 micro-rod, the dark current does not change obviously, but the photo-currents are significant enhanced. Under 532 nm illumination (Figure 5(a)), the photo-current is significantly enhanced to –15.82 μA at – 10 V (14.26 mW/cm^2) which is nearly four times that of the Sb_2Se_3 micro-rod photodetector under similar conditions. Response and recovery times (Figure 5(b)) show no obvious change. When irradiated with 980 nm laser, the photo-current further increase, up to –96 μA (42.56 mW/cm^2) which is nearly six times that of the Sb_2Se_3 micro-rod photodetector, with switching "ON/OFF" ratio as high as 50. As shown in Figure 5(e) the photo-response region has been extended to 1319 nm. A photo-current of about –5 μA at – 10 V is generated under the irradiation of 1319 nm laser (14.84 mW/cm^2). (No obvious difference can be observed between dark- and photo-currents under 1319 nm laser irradiation). It evidences that the $Sb_{2-x}Sn_xSe_3$ micro-rods has the extending NIR photo-response range. Meanwhile, the as-synthesized $Sb_{2-x}Sn_xSe_3$ micro-rods

could introduce the interfacial states, deep states and dangling bonds, which can trap one particular type of charge carrier, further decreasing the overall recombination of electron–hole pairs[23 - 25]. Therefore, the $Sb_{2-x}Sn_xSe_3$ micro-rod photodetector have an increasing photocarrier lifetimes and external quantum efficiencies (EQE). Furthermore, the response and recovery times at 1319 nm are greatly reduced, which are 0.08 s and 0.09 s, respectively. At the bias of –10 V, the time-resolved photo-response behaviours of the $Sb_{2-x}Sn_xSe_3$ device was comparatively investigated (Figure S2(c-e)). This result demonstrates the good stability of the $Sb_{2-x}Sn_xSe_3$ micro-rod photodetectors.

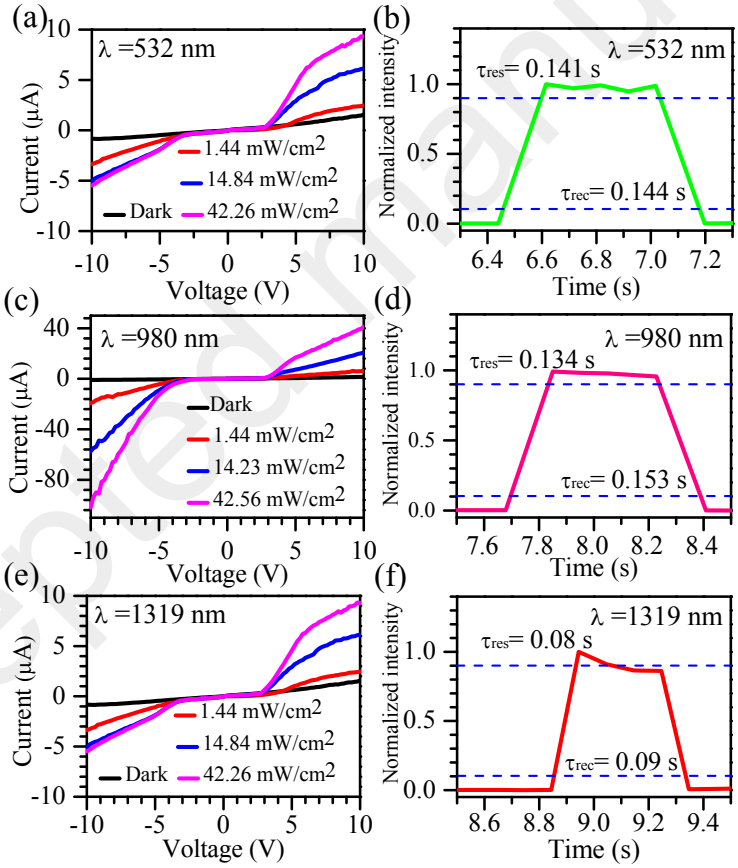

Figure 5. Photoconductive performance of the photodetector based on the single $Sb_{2-x}Sn_xSe_3$ micro-rod. (a) Dark current and photo-currents under 532 nm irradiation with different incident power densities; (b) An "on/off" cycle under 532 nm irradiation with 70.56 mW/cm^2 power density to show response and recovery time at a bias of 10V; (c) Dark current and photo-currents under 980 nm irradiation with different incident power densities; (d) An "on/off" cycle under 980 nm

irradiation with 70 mW/cm^2 power density to show response and recovery time at a bias of 10V; (e) Dark current and photo-currents under 1319 nm irradiation with different incident power densities; (f) An "on/off" cycle under 1319 nm irradiation with 70.64 mW/cm^2 power density to show response and recovery time at a bias of 10V.

The responsivity (R_{res}) is critical parameter for a photodetector, and it can be defined as the real photo-current (ΔI) generated per unit power of incident light on the unit effective area of a photodetector,

$$\boldsymbol{R_{res} = \Delta I / (P \cdot S)} \quad (3)$$

where $\Delta I = I_{illumination} - I_{dark}$, P is the incident light intensity and S is the effective illuminated area[26, 27]. The external quantum efficiency (EQE) and the spectral detectivity (D^*) could be calculated using the following equations:

$$\boldsymbol{EQE = hc \cdot R_{res}/(e \cdot \lambda)}, \quad (4)$$

$$\boldsymbol{D^* = R_{res}/(2e \cdot J_d)^{1/2}}, \quad (5)$$

where h is Planck's constant, c is the velocity of light, R_{res} is the responsivity, e is the electron charge, λ is the wavelength, and J_d is the dark current[27]. Given its well-arranged single crystalline microstructure, special 1D morphology, and high carrier concentration, the $Sb_{2-x}Sn_xSe_3$ micro-rod-based photodetector eventually obtains an ultra-high responsivity. For the single-micro-rod Sb_2Se_3 photodetector, its responsivity was calculated to be about 8.75×10^3 A·W^{-1} (0.504 mW/cm^2 at 532 nm) and 9.93×10^3 A·W^{-1} (1.44 mW/cm^2 at 980 nm). For the single $Sb_{2-x}Sn_xSe_3$ micro-rod photodetector, the responsivities were evaluated as 1.40×10^4 A·W^{-1} (0.504 mW·cm^{-2} at 532 nm, the corresponding EQE (3.27×10^6 %) and D^*(1.97×10^{16} Jones)) and 1.84×10^4 A·W^{-1} (1.44 mW/cm^2 at 980 nm, the corresponding EQE (2.33×10^6 %) and D^*(9.34×10^{16} Jones)), and the detailed values are listed in Table S1. Those values are about two times higher than those

of the single Sb_2Se_3 micro-rod-based photodetector. Table 2 summarizes the key parameters of the present single $Sb_{2-x}Sn_xSe_3$ micro-rod photodetector as well as some previously reported typical photodetectors. The photo-electronic properties reported in this work are comparable to the previously reported for the Sb_2Se_3-based photodetectors.[4, 8, 9, 28-33] Notably, the responsivity of the present $Sb_{2-x}Sn_xSe_3$ micro-rod photodetector is higher and its spectral response range is much broader than those of most previously reported Sb_2Se_3-based photodetectors.

Table 2. Performance comparison between the $Sb_{2-x}Sn_xSe_3$ micro-rod-based and other typical material-based photodetectors.

Photodetectors	**Wavelength**	**Response time (s)**	**Responsivity ($A \cdot W^{-1}$)**	**Reference**
Silicon	830 nm	~ ns	0.24	28
Graphene	1550 nm	~ ps	5×10^{-4}	29
Graphene–silicon heterojunction	850 ~ 900 nm	~ ms	0.435	30
MoS_2 mono-layer	< 700 nm	4/9	880	31
InSe multi-layer	633 nm	<0.05/<0.06	~ 7.0	32
Sb_2Se_3 nano-rod film	850 nm	0.7/1.1	0.015	4
$Sb_2Se_3/AgSbSe_2$ heterojunction film	850 nm	0.6/2.7	0.038	4
Sb_2Se_3 nano-wire	600 nm	< 0.3	~ 8.0	8
$(Sb_{1-x}Bi_x)_2Se_3$ nano-wire	639 nm	< 0.3/< 0.5	8.26×10^3	9
$SnSe_2$ micro-flake film	530 nm	0.015/0.008	1.10×10^3	33
$Sb_{2-x}Sn_xSe_3$ micro-rod	532 nm	0.117/0.078	1.40×10^4	This work
$Sb_{2-x}Sn_xSe_3$ micro-rod	980 nm	0.134/0.153	1.84×10^4	This work

CONCLUSION

Single-crystalline $Sb_{2-x}Sn_xSe_3$ micro-rods with a length of 20 ~ 30 μm were prepared from Sb_2Se_3 micro-rods through a hot-injection based Sn/Sb substitution strategy. The introduction of Sn firstly rendered the $Sb_{2-x}Sn_xSe_3$ micro-rods p-type with higher electrical conductivity ($1.65 \times 10^{-4}\ \Omega^{-1}\cdot m^{-1}$) and carrier concentrations ($6.139 \times 10^{13}\ cm^{-3}$) than Sb_2Se_3 micro-rods. In addition, introducing Sn red shifts the band gap of the $Sb_{2-x}Sn_xSe_3$ micro-rods to about 0.97 eV. Accordingly, the $Sb_{2-x}Sn_xSe_3$ micro-rods exhibit a broad-range photo-response from the visible to NIR spectral range. The micro-scale device based on a single $Sb_{2-x}Sn_xSe_3$ micro-rod shows a remarkable photodetecting performance with long-term durability, where the responsivity to 980 nm light (at 1.44 mW/cm^2 power density) reaches up to $1.84 \times 10^4\ A\cdot W^{-1}$, the external quantum efficiency is as high as 2.33×10^6 %, and the response/recovery time is as short as 0.134 s/0.153 s. The responsivity of the $Sb_{2-x}Sn_xSe_3$ micro-rod photodetector is about 2 times higher than that of the Sb_2Se_3-based one. Given its large photo-current, high responsivity, and short response/recovery time, the single $Sb_{2-x}Sn_xSe_3$ micro-rod based photodetector is a promising material for micro-photodetector applications.

AUTHOR INFORMATION

Corresponding Author

* E-mails: X. Qiao (qiaoxus@zju.edu.cn); X. Yang (yangxu-isee@zju.edu.cn); X. Fan (fanxp@zju.edu.cn); Tel.: +86-571-87951234.

SUPPORTING INFORMATION

Figure S1. TEM and EDXS of the Sb_2Se_3 micro-rod; **Figure S2.** Time-resolved photoresponse of Sb_2Se_3 micro-rod based photodetector; **Table S1** Responsivities; **Table S2-S3** Average response /recovery times with error bars.

REFERENCES

1. Kolmakov, A.; Moskovits, M., Chemical Sensing and Catalysis by One-Dimensional Metal-Oxide Nanostructures. *Annual Review of Materials Research* **2004**, *34*, 151-180.

2. Zhao, W.; Liu, L.; Xu, M.; Wang, X.; Zhang, T.; Wang, Y.; Zhang, Z.; Qin, S.; Liu, Z., Single Cds Nanorod for High Responsivity Uv-Visible Photodetector. *Advanced Optical Materials* **2017**, *5*, 1700159.

3. Mandl, M.; Wang, X.; Schimpke, T.; Kölper, C.; Binder, M.; Ledig, J.; Waag, A.; Kong, X.; Trampert, A.; Bertram, F. et al., Group Iii Nitride Core-Shell Nano- and Microrods for Optoelectronic Applications. *physica status solidi (RRL) - Rapid Research Letters* **2013**, *7*, 800-814.

4. Chen, S.; Qiao, X.; Wang, F.; Luo, Q.; Zhang, X.; Wan, X.; Xu, Y.; Fan, X., Facile Synthesis of Hybrid Nanorods with the $Sb_2Se_3/AgSbSe_2$ Heterojunction Structure for High Performance Photodetectors. *Nanoscale* **2016**, *8*, 2277-83.

5. Choi, D.; Jang, Y.; Lee, J.; Jeong, G. H.; Whang, D.; Hwang, S. W.; Cho, K. S.; Kim, S. W., Diameter-Controlled and Surface-Modified Sb_2Se_3 Nanowires and Their Photodetector Performance. *Scientific reports* **2014**, *4*, 6714.

6. Deng, Z.; Mansuripur, M.; Muscat, A. J., Simple Colloidal Synthesis of Single-Crystal Sb-Se-S Nanotubes with Composition Dependent Band-Gap Energy in the near-Infrared. *Nano Letters* **2009**, *9*, 2015-2020.

7. Zhou, Y.; Wang, L.; Chen, S.; Qin, S.; Liu, X.; Chen, J.; Xue, D.-J.; Luo, M.; Cao, Y.; Cheng, Y. et al., Thin-Film Sb_2Se_3 Photovoltaics with Oriented One-Dimensional Ribbons and Benign Grain Boundaries. *Nature Photonics* **2015**, *9*, 409-415.

8. Zhai, T.; Ye, M.; Li, L.; Fang, X.; Liao, M.; Li, Y.; Koide, Y.; Bando, Y.; Golberg, D., Single-Crystalline Sb_2Se_3 Nanowires for High-Performance Field Emitters and Photodetectors. *Advanced materials* **2010**, *22*, 4530-3.

9. Huang, R.; Zhang, J.; Wei, F.; Shi, L.; Kong, T.; Cheng, G., Ultrahigh Responsivity of Ternary Sb-Bi-Se Nanowire Photodetectors. *Advanced Functional Materials* **2014**, *24*, 3581-3586.

10. Zhang, X.; Xu, Y.; Shen, Q.; Fan, B.; Qiao, X.; Fan, X.; Yang, H.; Luo, Q.; Calvez, L.; Ma, H. et al. Enhancement of Charge Photo-Generation and Transport Via an Internal Network of Sb_2Se_3/Cu_2GeSe_3 heterojunctions. *J. Mater. Chem. A* **2014**, *2*, 17099-17106.

11. Lupan, O.; Cretu, V.; Postica, V.; Ahmadi, M.; Cuenya, B. R.; Chow, L.; Tiginyanu, I.; Viana, B.; Pauporté, T.; Adelung, R. Silver-doped zinc oxide single nanowire multifunctional nanosensor with a significant enhancement in response. *Sensors and Actuators B: Chemical* **2016,** *223*, 893-903.

12. Chen, S.; Qiao, X.; Zheng, Z.; Cathelinaud, M.; Ma, H.; Fan, X.; Zhang, X., Enhanced Electrical Conductivity and Photoconductive Properties of Sn- Doped Sb_2Se_3 Crystals. *Journal of Materials Chemistry C* **2018**, *6*, 6465-6470.

13. M.S. Iovu ; S.D. Shutov ; V.I. Arkhipov ; Adriaenssens, G. J. Effect of Sn doping on photoconductivity in amorphous As_2Se_3 and AsSe films. *Journal of Non-Crystalline Solids* **2002,** *299-302*, 1008-1032.

14. Ankit Kumar Pandey ; Rikmantra Basu; Chang, G.-E. Optimized $Ge_{1-x}Sn_x$/Ge Multiple-Quantum-Well Heterojunction Phototransistors for High-Performance SWIR Photodetection. *IEEE SENSORS JOURNAL* **2018,** *18*, 5842-5852.

15. Zhang, C.; Yin, H.; Han, M.; Dai, Z.; Pang, H.; Zheng, Y.; Lan, Y. Q.; Bao, J.; Zhu, J., Two-Dimensional Tin Selenide Nanostructures for Flexible All-Solid-State Supercapacitors. *ACS nano* **2014**, *8*, 3761-70.

16. Pauling, L., Atomic Radii and Interatomic Distances in Metals. *Journal of the American Chemical Society* **1947**, *69*, 542-553.

17. Volobujeva, O.; Mellikov, E.; Timmo, K.; Danilson, M.; Bereznev, S., $Cu_2ZnSnSe_4$ Films from Binary Precursors. *Journal of Renewable and Sustainable Energy* **2013**, *5*, 031618.

18. Ling, C.; Huang, Y.; Liu, H.; Wang, S.; Fang, Z.; Ning, L., Mechanical Properties, Electronic Structures, and Potential Applications in Lithium Ion Batteries: A First-Principles Study toward $SnSe_2$ Nanotubes. *The Journal of Physical Chemistry C* **2014**, *118*, 28291-28298.

19. Chen, G.; Wang, W.; Wang, C.; Ding, T.; Yang, Q., Controlled Synthesis of Ultrathin Sb_2Se_3 Nanowires and Application for Flexible Photodetectors. *Advanced science* **2015**, *2*, 1500109.

20. Liu, Y.-Q.; Zhang, M.; Wang, F.-X.; Pan, G.-B., Facile Microwave-Assisted Synthesis of Uniform Sb_2Se_3nanowires for High Performance Photodetectors. *J. Mater. Chem. C* **2014**, *2*, 240-244.

21. LaPierre, R. R.; Robson, M.; Azizur-Rahman, K. M.; Kuyanov, P., A Review of Iii – V Nanowire Infrared Photodetectors and Sensors. *Journal of Physics D: Applied Physics* **2017**, *50*, 123001.

22. Soci, C.; Zhang, A.; Bao, X.-Y.; Kim, H.; Lo, Y.; Wang, D., Nanowire Photodetectors. *Journal of Nanoscience and Nanotechnology* **2010**, *10*, 1430-1449.

23. Spray, R. L.; McDonald, K. J.; Choi, K.-S. Enhancing Photoresponse of Nanoparticulate α- Fe_2O_3 Electrodes by Surface Composition Tuning. *The Journal of Physical Chemistry C* **2011,** *115*, 3497-3506.

24. Zhou, W.; Peng, Y.; Yin, Y.; Zhou, Y.; Zhang, Y.; Tang, D. Broad spectral response photodetector based on individual tin-doped CdS nanowire. *AIP Advances* **2014,** *4*, 123005.

25. Zhang, K.; Luo, T.; Chen, H.; Lou, Z.; Shen, G. Au-nanoparticles-decorated Sb_2S_3 nanowire-based flexible ultraviolet/visible photodetectors. *Journal of Materials Chemistry C* **2017,** *5*, 3330-3335.

26. Wang, X.; Tian, W.; Liao, M.; Bando, Y.; Golberg, D. Recent advances in solution-processed inorganic nanofilm photodetectors. *Chemical Society reviews* **2014,** *43*, 1400-22; 27. Teng, F.; Hu, K.; Ouyang, W.; Fang, X. Photoelectric Detectors Based on Inorganic p-Type Semiconductor Materials. *Advanced materials* **2018,** *30*, e1706262

28. Huang, Z.; Carey, J. E.; Liu, M.; Guo, X.; Mazur, E.; Campbell, J. C., Microstructured Silicon Photodetector. *Applied Physics Letters* **2006**, *89*, 033506.

29. Xia, F.; Mueller, T.; Lin, Y.-m.; Valdes-Garcia, A.; Avouris, P., Ultrafast Graphene Photodetector. *Nature nanotechnology* **2009**, *4*, 839-843.

30. An, X.; Liu, F.; Jung, Y. J.; Kar, S., Tunable Graphene-Silicon Heterojunctions for Ultrasensitive Photodetection. *Nano letters* **2013**, *13*, 909-16.

31. Lopez-Sanchez, O.; Lembke, D.; Kayci, M.; Radenovic, A.; Kis, A., Ultrasensitive Photodetectors Based on Monolayer MoS_2. *Nature nanotechnology* **2013**, *8*, 497-501.

32. Tamalampudi, S. R.; Lu, Y. Y.; Kumar, U. R.; Sankar, R.; Liao, C. D.; Moorthy, B. K.; Cheng, C. H.; Chou, F. C.; Chen, Y. T., High Performance and Bendable Few-Layered Inse Photodetectors with Broad Spectral Response. *Nano letters* **2014**, *14*, 2800-6.

33. Jang, K.; Lee, I.-y.; Xu, J.; Choi, J.; Jin, J.; Park, J. H.; Kim, H. J.; Kim, G.-H.; Son, S. U. Colloidal Synthesis of SnSe Nanocolumns through Tin Precursor Chemistry and Their Optoelectrical Properties. *Crystal Growth & Design* **2012,** *12*, 3388-3391

TOC Graphic

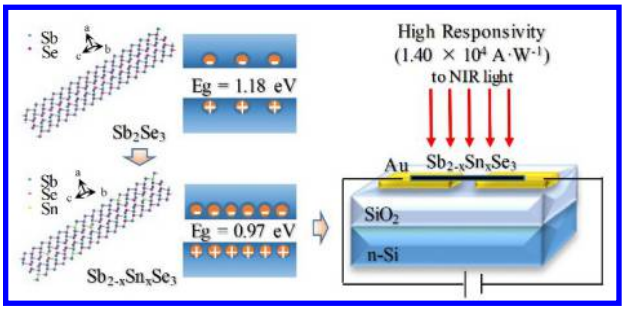

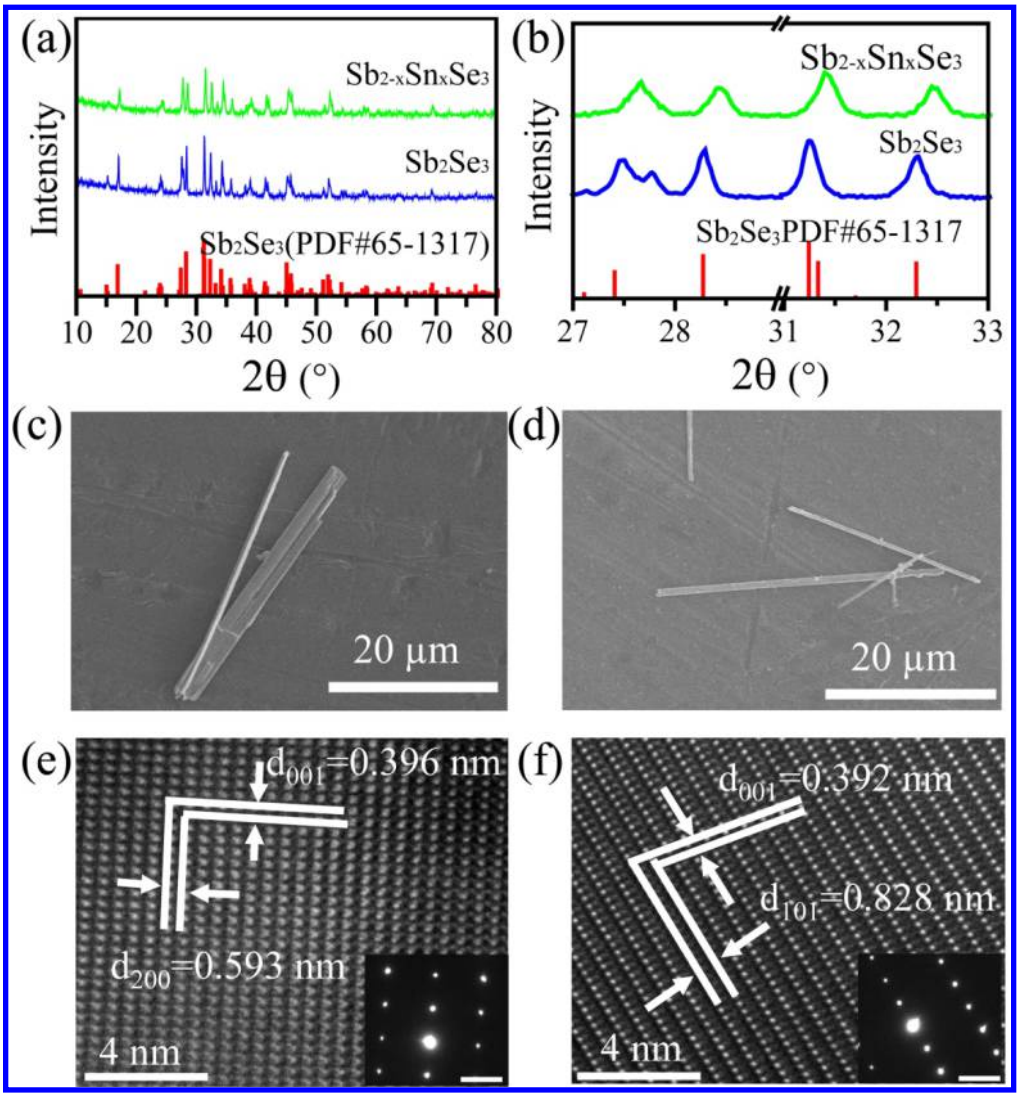

Figure 1 (a) XRD patterns of Sb_2Se_3 micro-rods and $Sb_{2-x}Sn_xSe_3$ micro-rods, (b) partial enlarged detail of figure (a); SEM image of (c) Sb_2Se_3 micro-rods and (d) $Sb_{2-x}Sn_xSe_3$ micro-rods; HRTEM image of (e) Sb_2Se_3 micro-rods and (f) $Sb_{2-x}Sn_xSe_3$ micro-rods. The insets are the electron diffraction patterns by Fast Fourier Transforming (FFT) of the selected area corresponding to (e) and (f), where the scale bars stand for 2 1/nm.

140x150mm (300 x 300 DPI)

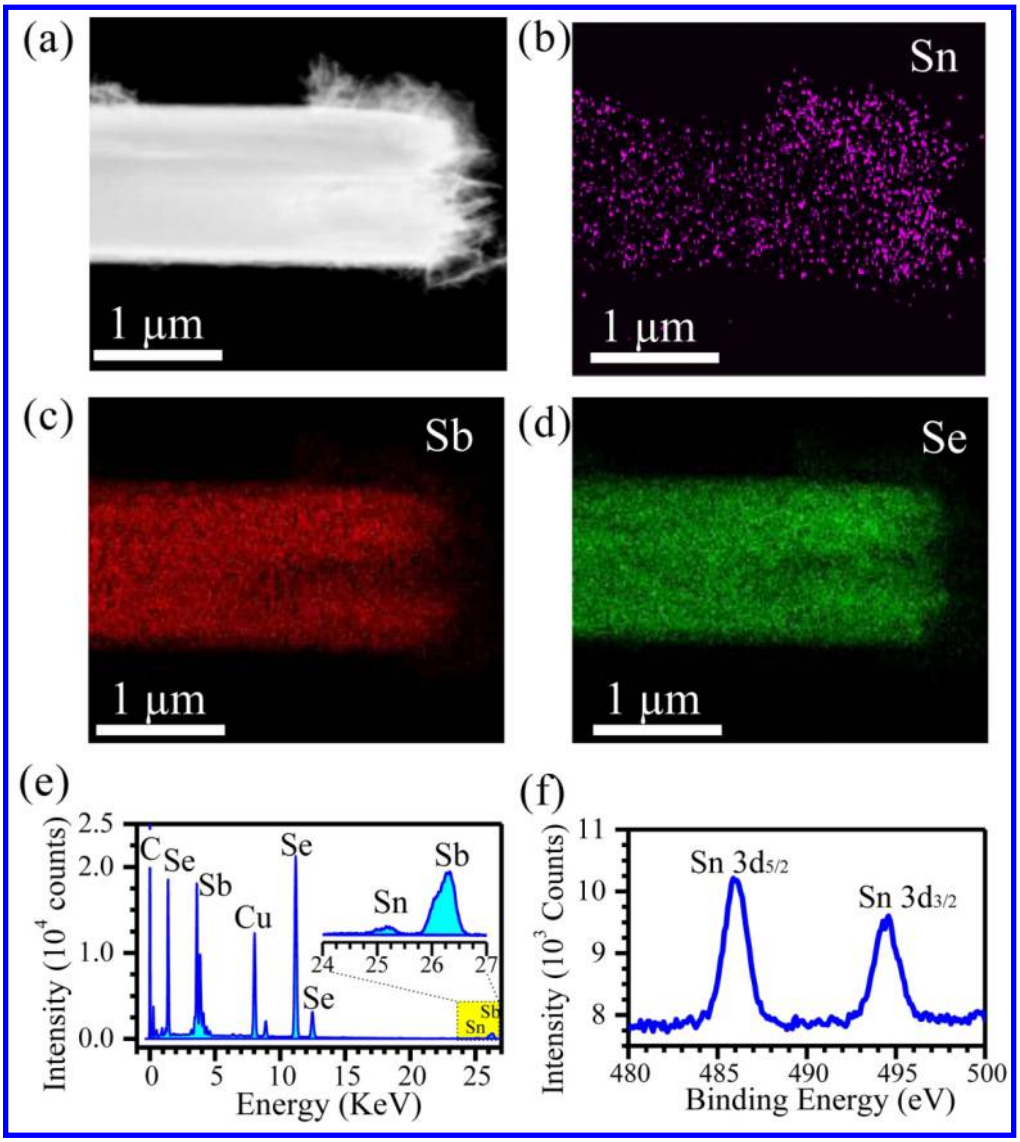

Figure 2 High Angle Annular Dark field (HAADF) image (a), EDX maps of Sn (b), Sb (c), and Se (d) elements, EDX spectrum (e) and XPS spectrum (f) of the single $Sb_{2-x}Sn_xSe_3$ micro-rod.

178x200mm (300 x 300 DPI)

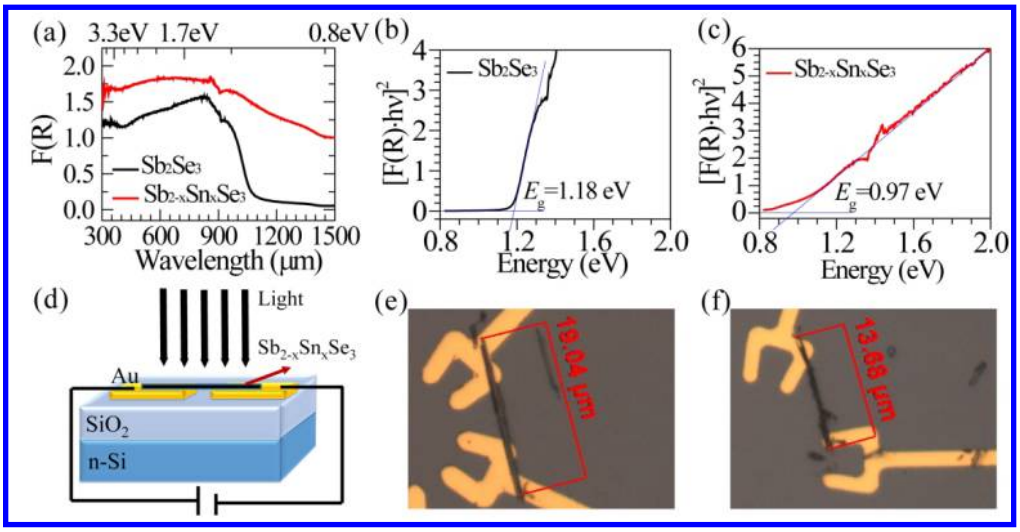

Figure 3 Optical absorption spectra (a) (calculated from the diffuse reflectance data) for Sb_2Se_3 and $Sb_{2-x}Sn_xSe_3$ micro-rods; a plot of $[F(R)\ h\nu]^2$ vs. energy for the Sb_2Se_3 micro-rods (b) and $Sb_{2-x}Sn_xSe_3$ micro-rods (c), from which band gap energy could be evaluated; schematic illustration of a single micro-rod photodetector (d); optical images of fabricated devices based on a single Sb_2Se_3 micro-rod (e) and based on a single $Sb_{2-x}Sn_xSe_3$ micro-rod (f).

210x107mm (300 x 300 DPI)

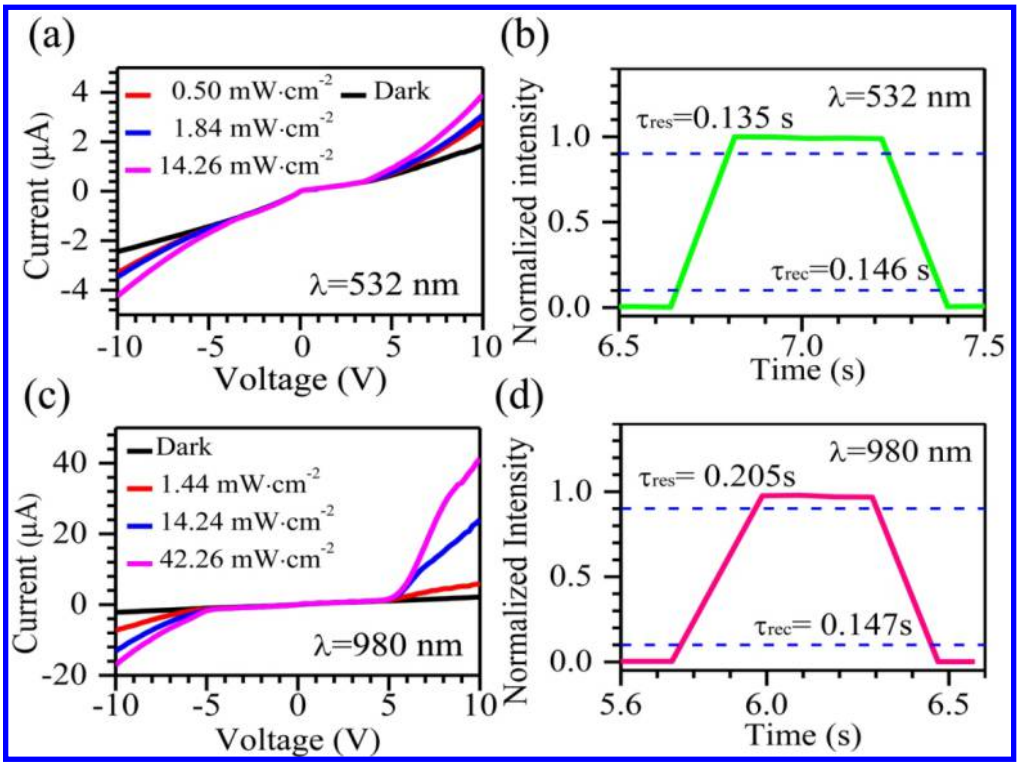

Figure 4 Photoconductive performance of the photo-detector based on the single Sb_2Se_3 micro-rod. (a) Dark current and photo-currents under 532 nm irradiation with different incident power densities; (b) An "ON/OFF" cycle under 532 nm irradiation with 71.35 mW•cm^{-2} power density to show response and recovery time at a bias of 10V; (c) Dark current and photo-currents under 980 nm irradiation with different incident power densities; (d) An "ON/OFF" cycle under 980 nm irradiation with 74.23 mW•cm^{-2} power density to show response and recovery time at a bias of 10 V.

119x88mm (300 x 300 DPI)

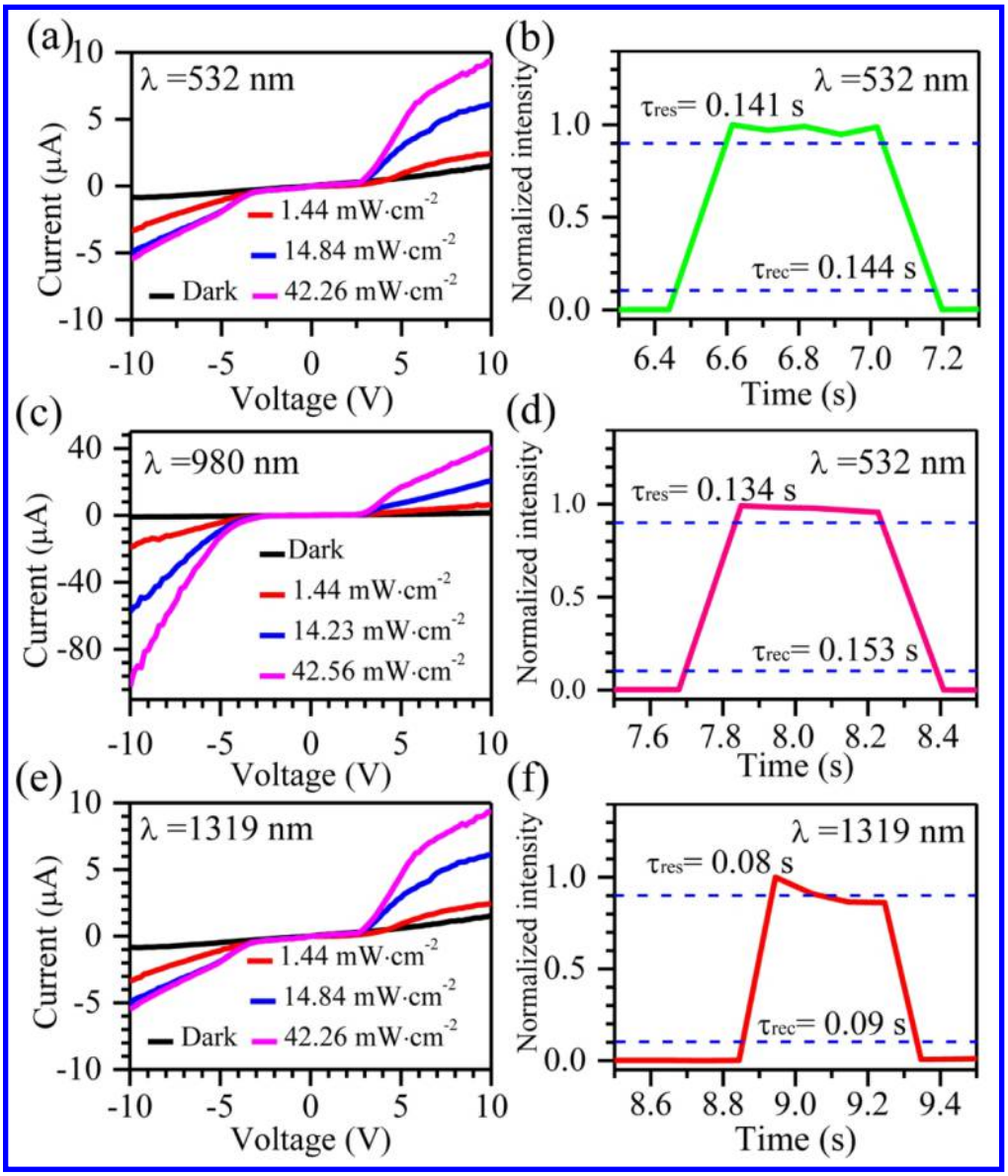

Figure 5 Photoconductive performance of the photo-detector based on the single $Sb_{2-x}Sn_xSe_3$ micro-rod. Dark current and photo-currents under 532 nm irradiation (a) , under 980 nm irradiation (c) and under 1319 nm irradiation (e) with different incident power densities. An "ON/OFF"" cycle under 532 nm irradiation with 70.56 mW•cm^{-2} power density (b), under 980 nm irradiation with 70 mW•cm^{-2} power density (d) and under 1319 nm irradiation with 70.64 mW•cm^{-2} power density (f) to show response and recovery time at a bias of 10 V.

187x218mm (300 x 300 DPI)

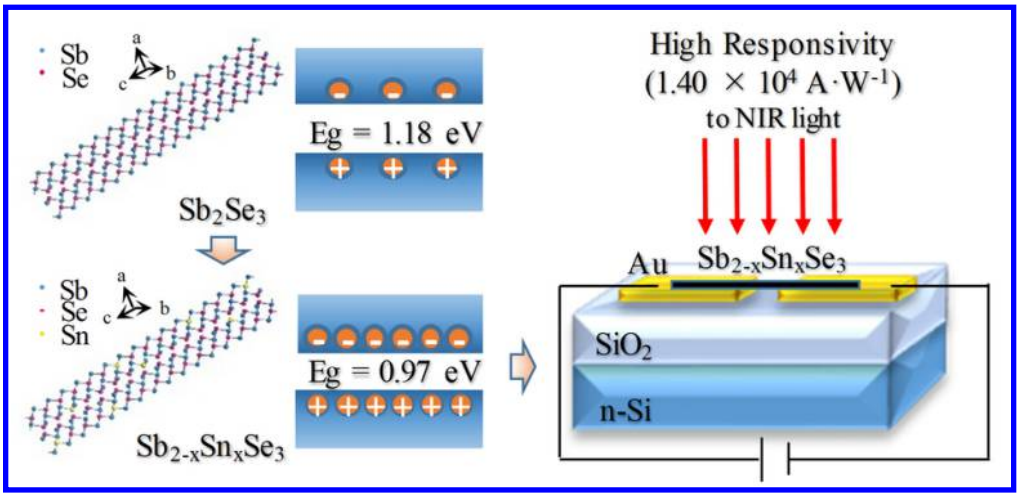

Table of Contents Graphic

80x38mm (300 x 300 DPI)